# Reinforcement learning entangling operations on spin qubits

Mohammad Abedi<sup>1, 2</sup> and Markus Schmitt<sup>1, 3</sup>

<sup>1</sup> PGI-8 (Quantum Control), Forschungszentrum Jülich, Wilhelm-Johnen-Straße, 52428, Jülich .

 $^2$ Fakultät für Physik, University of Regensburg, Universitätsstraße 31, D-93051, Regensburg .

<sup>3</sup>Fakultät für Informatik und Data Science, University of Regensburg, Universitätsstraße 31, D-93040, Regensburg.

Contributing authors: m.abedi@fz-juelich.de; mar.schmitt@fz-juelich.de;

#### Abstract

High-fidelity control of one- and two-qubit gates past the error correction threshold is an essential ingredient for scalable quantum computing. We present a reinforcement learning (RL) approach to find entangling protocols for semiconductor-based singlet-triplet qubits in a double quantum dot. Despite the presence of realistically modelled experimental constraints, such as various noise contributions and finite rise-time effects, we demonstrate that an RL agent can yield performative protocols, while avoiding the model-biases of traditional gradient-based methods. We optimise our RL approach for different regimes and tasks, including training from simulated process tomography reconstruction of unitary gates, and investigate the nuances of RL agent design.

**Keywords:** quantum control, reinforcement learning, RL, quantum dots, quantum computing, machine learning

#### 1 Introduction

Quantum technology is a rapidly growing research field with extensive crossdisciplinary interests. Its applications for computation is conditioned on the implementation of accurate logic gates. Two facets of this requirement are the development of quantum hardware with fast, scalable coherent dynamics, and the ability to steer and manipulate the system to implement arbitrary logical operations, even in the presence of decohering noise. The theory of quantum control (QC) and quantum optimal control (QOC) [1–3] has provided the theoretical framework for the latter task. A typical approach to (optimal) quantum control usually involves optimisation through the computation of gradients of a Hamiltonian [4–7]. Although this approach is efficient, it's stipulated on the accuracy of the model (i.e. its Hamiltonian description) and, in the case of real quantum environments, on the validity of a noise description. Such model bias may cause gradient-based optimisation to perform sub-optimally or converge to a local minimum.

In recent years, reinforcement learning (RL) [8] has swiftly developed into a general framework for (optimal) control and interactive learning tasks with a diverse domain of utilisation such as autonomous driving [9], robotics [10], fine-tuning large-language-models with human feedback [11], and learning to play games such as Chess and Go [12]. This set of algorithms is deployed to optimise sequential decision-making and maximise cumulative feedback. No prior knowledge of the underlying system is required, since learning and experience are achieved simultaneously through an interactive process between an agent and its environment. These model-free (i.e. Hamiltonian-free) approaches have already successfully been implemented in the context of QC [13–21]. However, there are a number of remaining important challenges that we investigate.

In contrast to classical control systems, the observation of a state in a quantum environment presents a fundamental limitation in the ability of environment-agent interactions since any (weak or otherwise) measurement perturbs the system. Alternatively, preparing many identical copies of a known initial state, followed by implementing a control protocol, and then conducting a complete measurement requires substantial experimental resources. This is because process tomography typically requires millions of measurements, even for a small qubit system [15, 22]. Further complications are certain experimental features in different quantum platforms such as delayed response to applied control, which, from the RL perspective, affects the Markovian properties of the problem. Additionally, decohering noise including time-correlated noise compounds with the statistical noise of measurement, adding a significant amount of uncertainty in the optimisation process.

Previous work in QC with RL included discrete-pulse optimisation of the IBM superconducting platform, finding more time-efficient gates with RL [15], synthesising noise-resilient pulses in gmon systems given knowledge of a noisy environment [16], constructing entangling gates on simulated transmon systems with continuous controls [17], and demonstrating agent-based learning ability to discover novel protocols compared to conventional ansätze. Other work includes synthesising unitaries with discrete-pulse sequences [18, 20], investigating optimal control protocols in different controllability regimes [19], and optimising control sequences of parameterised circuits to generate desired gates with measurement feedback [21]. Another investigation used RL ansätze with a Hamiltonian-gradient-based approach to yield improved fidelities [23]. Our work is in the spirit of these efforts and our aim is to further bridge the gap between comparatively abstract control models and a viable quantum platform that contains the diverse nuances expected of an experimental device.

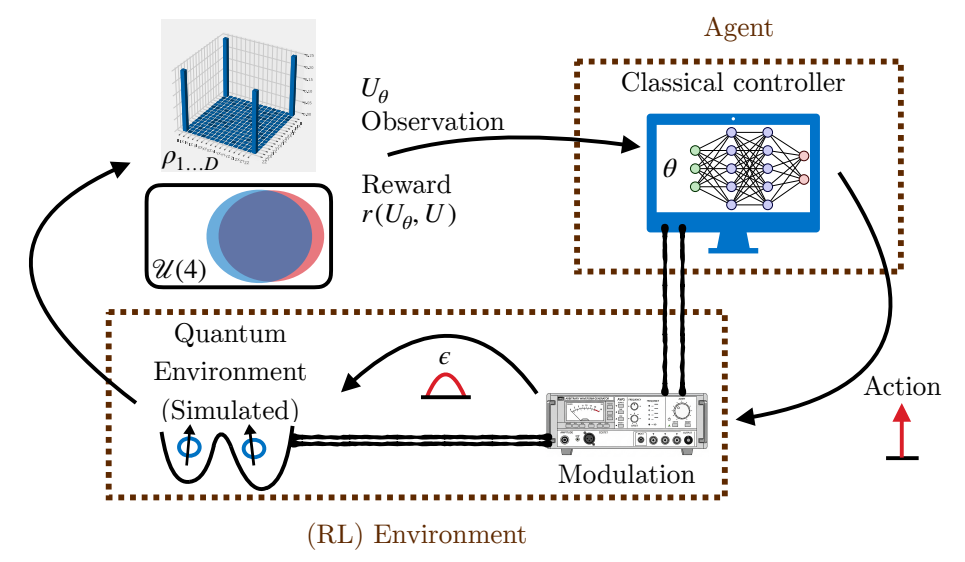


Fig. 1 The interaction loop of reinforcement learning (RL) applied to quantum control (QC). An RL agent (i.e. a neural network in a classical computer) outputs a continuous number within a bounded interval (i.e. an action) in instant time. Due to finite-rise effects and ringing of controlled hardware, the action is convolved with a measured impulse response function to better represent the model dynamics. The double quantum dot system is then perturbed using a Trotterised decomposition scheme. Feedback is provided to the agent in the form of an observation characterizing an implicit action-evolution correlation, and a reward representing an observation-action dependent goal. An observation consists of either complete or limited (e.g. process tomography) information about the current generated unitary, while a reward is a function of the current unitary and a target gate. Finally, the agent outputs a new feedback-dependent action.

As a concrete example, we will consider semiconductor-based spin qubits [24] and in particular singlet-triplet qubits [25, 26]. Platforms based on spin qubits are a suitable candidate for quantum computing as they have long coherence times [27, 28], experimentally demonstrated gate fidelities past the error correction threshold for both one and two qubit gates [29, 30], allow for fast electrical control [26], and are scalable due to existing knowledge in industrial fabrication [31]. A sophisticated gradient-based approach to design optimal entangling operations using a detailed model including the relevant device imperfections has been developed previously by Cerfontaine et al. [26], providing a competitive benchmark for our RL approach. Furthermore, although not the focus of our investigation, closed-loop control with fine-tuning with experimental data has been performed for GaAs qubits [32]. Future work could incorporate some or all parts of this workflow with RL agents.

We examine the design choices of RL agents and their impact on performance, emphasising moving towards a practical approach to quantum control. These choices are informed by the experimental features of finite-rise times, multiple sources of decohering noise, and shot noise. Such design choices include exploring model- and history-of-action-based belief states to learn noise-robust entangling strategies. We

aim to find solutions that exceed the accuracy of the gradient-based approach, sequentially surveying the experimental aspects of a quantum dot platform, with increasing complexity.

In the following, we will first introduce the details of the physical platform in Section 2 and basics of RL in Section 3, before presenting the results in Section 4.

## 2 Quantum Dots

We present a brief overview of the quantum platform that is optimised. Readers interested in the full experimental details are referred to [25, 26]. One- and two-qubit gates were previously synthesised using the filter function formalism [33] and the gradient-based Levenberg–Marquardt algorithm to optimise pulses which minimise the average gate infidelity. Our interest in testing optimal controllability of this particular model with an RL agent is motivated by experimental constraints of noise and finite rise-time effects which provide additional challenges in the learning process, and the availability of a comparative benchmark [26].

This singlet-triplet qubit system consists of four adjacent, confined quantum dots in a semiconducting GaAs heterostructure (Fig. 2 (a)) which are used to encode a (logical) two-qubit system. The system is described by the following Hamiltonian, given in units of angular frequencies ( $\hbar = 1$ ):

$$H = \sum_{i}^{3} \frac{J(\epsilon_{i,i+1})}{4} \overline{\sigma}^{(i)} \cdot \overline{\sigma}^{(i+1)}$$

$$+ \frac{B_G}{2} \sum_{i}^{4} \sigma_z^{(i)}$$

$$+ \frac{b_{12}}{8} \left( -3\sigma_z^{(1)} + \sigma_z^{(2)} + \sigma_z^{(3)} + \sigma_z^{(4)} \right)$$

$$+ \frac{b_{23}}{4} \left( -\sigma_z^{(1)} - \sigma_z^{(2)} + \sigma_z^{(3)} + \sigma_z^{(4)} \right)$$

$$+ \frac{b_{34}}{8} \left( -\sigma_z^{(1)} - \sigma_z^{(2)} - \sigma_z^{(3)} + 3\sigma_z^{(4)} \right)$$

$$(1)$$

Here,  $\sigma_a^{(i)}$  is the Pauli operator that acts on the quantum dot with label i. Each spin experiences a constant magnetic field  $B_i$ .  $B_G = \sum_i B_i$  is the mean field and  $b_{ij} = B_i - B_j$  represents the magnetic gradient across adjacent dots. Application of an external magnetic field energetically splits the six states with  $m_s = 0$  and those with non-zero magnetic moment. These six states are further split into a computational subspace:

$$\begin{cases}
|00\rangle := |\uparrow\downarrow\uparrow\downarrow\rangle & |01\rangle := |\uparrow\downarrow\downarrow\uparrow\rangle \\
|10\rangle := |\downarrow\uparrow\uparrow\downarrow\rangle & |11\rangle := |\downarrow\uparrow\downarrow\uparrow\rangle
\end{cases}$$
(2)

Additionally, there are two inter-double dot leakage states accessible via  $J_{23}$ :

$$\{|L_1\rangle := |\uparrow\uparrow\downarrow\downarrow\rangle \quad |L_2\rangle := |\downarrow\downarrow\uparrow\uparrow\rangle \} \tag{3}$$

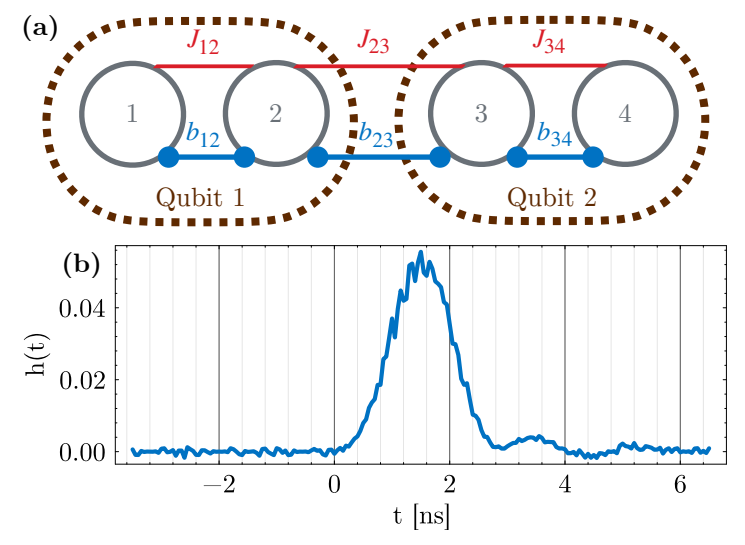


Fig. 2 (a) A two-qubit system using four adjacent electron spins in a semiconducting heterostructure. Voltage pulses between dots are controlled to modify the strength of the exchange interactions  $J_{ij}$ , affecting the occupation levels of computational subspace.  $b_{ij} = B_i - B_j$  are the average magnetic field gradients across dots (i, j), and  $\frac{1}{4} \sum_i B_i = B_G$  gives the total applied external magnetic field. (b) The kernel used to convolve piecewise-constant pulses creating smoothened pulses which more accurately describe the qubit dynamics. Notably, there is a ~1ns delay from the input by the controller. This is relevant when the inputs are sent in less than this time, as it can cause symbol interference.

Detuning voltage pulses  $\epsilon_{ij}$  are used to affect the energy difference between adjacent dots, controlling the exchange interaction  $J_{ij}$ , which is modelled as  $J_{ij} = J_0 \exp\left(\frac{\epsilon_{ij}}{\epsilon_0}\right)$ , where  $J_0, \epsilon_0$  are the base units of this system, given in ns and meV respectively.

 $\epsilon_{ij}(t)$  is controlled by an arbitrary waveform generator (AWG) which is constrained by amplitude bounds as well as a fixed sample period  $T_s$ , producing piecewise-constant pulses. Furthermore, the finite bandwidth of the system combined with ringing of the control hardware is modelled by the use of a convolution filter smoothening piecewise-constant pulses

$$\epsilon'_{ij}(t) = \int_0^t \epsilon_{ij}(t)h(t - t')dt' \tag{4}$$

where h(t) is the convolution kernel. We use the measured impulse response function (Fig. 2 (b)) as our convolution kernel. This was obtained by digitising data from Cerfontaine  $et\ al.\ [26]$ , which was constructed with the following procedure: A square pulse was sent to the device as an input via an AWG through a series of low-loss cables. This yielded a measured distorted square pulse, and the time-derivative of the resulting step response corresponds to the impulse response function. This impulse response function is used to convolute the input pulses in our model.

Three noise contributions to the system are included in the optimisation procedure. One of these is the quasi-static hyperfine noise on drift mean magnetic field gradients

<sup>&</sup>lt;sup>1</sup>As an alternative, the impulse response function can be measured directly using instant (Dirac-delta) pulses, whose integral corresponds to the step response.

 $b_{ij}$ . This noise fluctuates on time scales slower than the protocol duration. Hence, it is modelled as a Gaussian noise with standard deviation  $\sigma_b$  for each individual protocol:

$$\tilde{b}_{ij} = b_{ij} + \delta_{b_{ij}}; \quad \delta_{b_{ij}} \sim \mathcal{N}(0, \sigma_b) \tag{5}$$

A similar slow charge noise with standard deviation  $\sigma_{\epsilon}$  contributes to one of two sources of noise on the detuning voltages  $\epsilon_{ij}$ . Furthermore, the decoherence noise from  $\epsilon_{ij}$  is also affected by fast (nanosecond scale) charge noise, and is modelled via a full noise spectrum of time-correlated coloured noise ( $\sim \frac{1}{f^{\alpha}}$  for frequency f). An optimistic scenario with minimal effects from high frequency regimes can be represented by taking  $\alpha=0.7$  and a pessimistic extreme is represented as  $\alpha=0.0$ , or white noise:

$$\tilde{\epsilon}_{ij}(t) = \epsilon'_{ij}(t) + \delta^1_{\epsilon'_{ij}} + \delta^2_{\epsilon'_{ij}}(t);$$

$$\delta^1_{\epsilon_{ij}} \sim \mathcal{N}(0, \ \sigma_{\epsilon}) \quad \delta^2_{\epsilon'_{ij}} \sim S_{\epsilon,\alpha}(f)$$
(6)

System parameters are given in terms of  $\epsilon_0$  for detuning voltages and  $J_0$  for magnetic field and exchange interactions. For a GaAs device, we use the previously used parameters [26] and set  $J_0=1 {\rm ns}^{-1}$  with  $b_{12}=-b_{34}=J_0$  and  $b_{23}=7J_0$  to suppress leakage by making the exchange interaction between the qubits costly [34]. Slow fluctuations on the magnetic field gradients are  $\sigma_b=0.0105J_0$ . The detuning pulses are constrained by the AWG with a rise time of  $\sim 1 {\rm ns}$  and are hence bounded to the interval  $[-5.4\epsilon_0, 2.4\epsilon_0]$  where  $\epsilon_0=0.272 {\rm mV}$  and include a slow charge contribution of standard deviation  $\sigma_\epsilon=0.0294\epsilon_0$ . The fast charge noise spectrum is extrapolated to  $4\times 10^{-20} {\rm V}^2 {\rm Hz}^{-1}$  at 1 MHz such that  $S_{\epsilon,\alpha}(f)=53.8\epsilon_0^2 {\rm ns}\left(\frac{1 {\rm Hz}}{f}\right)^\alpha$ .

For optimisation, we train an agent with a numerically simulated quantum dot environment. We aim to find control pulses that construct an entangling gate, CNOT, in the logical basis with a synthesised and discretised sequence of detuning pulses  $\{\epsilon_{ij,t}\}_{t=0}^{t=N}$  generated in some finite time T consisting of N segments. This gives a sample period for the AWG as  $T_s = \frac{T}{N}$ .

In our numerical simulation of the device dynamics, the unitary is generated using the Trotterised evolution of the Hamiltonian (1). The accuracy of the discretised time evolution is given by the time step,  $\mathcal{O}(\delta t^2)$ , and is chosen to be sufficiently small to mitigate discretisation errors. By oversampling the pulses n times (i.e. for each input, there are n substeps), we produce increasingly smoother convoluted traces of the input pulses (4) and fix the time step as  $\delta t = T_s/n = T/Nn$  with the approximate time evolution operator  $U(t) = \prod_{m=0}^{M} \exp\left(-i\delta t H(\epsilon'_{ij,m})\right)$  for M = Nn steps and shaped (i.e. convoluted) pulses  $\epsilon'_{ij,m}$ . For each step, we have  $U_m = \exp\left(-i\delta t H(\epsilon'_{ij,m})\right)U_{m-1}$  and  $U_0 = 1$ . Note to distinguish the input sequence discretisation, which is labelled by  $t = 1 \dots Nn$ . (i.e. the input unshaped pulse amplitudes), from the numerical simulation (including oversampling), which is labelled by  $m = 1 \dots Nn$ .

Furthermore, we fix the final four segments at their minimum value to ensure each protocol ends with minimal exchange interaction. This is an enforced constraint on the optimisation procedure, giving us N-4 choices of pulse amplitudes.

RL	Quantum Control	
Observation $o_t$	Pulse history $\epsilon_{o:t}$ and / or unitary gate $U_t$ (potentially estimated with process tomography statistics), and time-to-go	
Belief $b_t$	A belief state over the underlying latent unitary conditioned on the history of actions and observations	
Action $a_t$	A real continuous value in a closed interval that is smeared via an AWG to become a pulse amplitude $\epsilon$	
Reward $r_t$	A function of the (estimated) gate fidelity (Eq. 7)	

Table 1 RL components and their quantum control aspects.

Taking into account the effects of finite rise time, noise contributions, and model simulation, we can now proceed to introduce the basic concepts of the RL optimisation algorithm.

## 3 Reinforcement Learning on Quantum Dots

We present a brief description of reinforcement learning (RL) and its formulation in the context of quantum dots. A more comprehensive overview is given in Appendix A, and Sutton & Barto [8].

In RL, an abstract agent or learning system receives feedback signals from its interactions with an environment, learning an optimal strategy or sequence of interactions to achieve a desired task. RL does not require expert supervision or knowledge distillation; an agent can learn directly from experience, and only needs to learn to maximise the feedback signal. A model of the environment is not explicitly required.

In the framework of Markov decision processes (MDPs) [8] underlying RL, an agent learns and interacts with an environment by taking actions  $a_t \in \mathcal{A}$  through a conditional probability distribution known as a policy  $\pi(a_t|s_t)$ , where  $s_t \in \mathcal{S}$  is a state of the environment. This action affects the environment state through a Markovian transition probability function  $\mathcal{T}(s_{t+1}|s_t,a_t)$ , giving a new state  $s_{t+1}$ . The agent then observes this updated state alongside a reward signal  $r_t$  from the environment and its goal is to learn a policy  $\pi^*$  that maximises the cumulative reward over a sequence of actions, the return. A sequence may be constructed to terminate upon reaching a particular state or after a fixed number of steps. A finite sequence is known as an episode and an agent may require many episodes to successfully learn an optimal strategy.

In quantum systems, direct access to the environment is limited due to the distinctive nature of measurement. Therefore we generalise the MDP framework to a partially observable Markov decision process (POMDPs) [8]. In addition to the set of states S, it includes an observation set O and an observation probability function

of getting an observation  $o_t$  given a state-action pair  $\mathcal{Z}(o_{t+1}|s_{t+1}, a_t)$ . This added stochasticity adds uncertainty to the agent's policy as a state model is additionally required. One choice of a state model is to maintain a history of actions and observations  $h_t = a_0 o_1 a_1 o_2 \dots a_{t-1} o_t$  which satisfies the Markovian property for being an RL state. However, due to potential intractability of histories for long sequences, a compact representation of the history known as a belief state  $b_t = f^*(h_t)$  is sufficient (albeit optimisation may be difficult). A belief state is then a probability distribution over the underlying states  $s_t$  conditioned on the history  $h_t$ .

The engineering of an RL loop is a non-trivial task and requires careful consideration of the state, action, and reward spaces to solve a desired task. We present an overview of our design choices for each category below and in Section 4. A summary is given in Table 1 and an overview can be seen in Fig. 1. A (classical) controller is constituted by a parameterised neural network policy  $\pi_{\theta}$  that outputs a continuous action in a closed interval between a chosen minimal and maximal pulse amplitude, conditioned on the obtained observation. This action is then passed to the quantum system through an AWG device, which constitutes a part of the RL environment dynamics. Finally, the system evolves under the simulated dynamics with Hamiltonian (Eq. 1) and noise (Eq. 6). This loop is repeated for a fixed number of time steps and we construct a protocol (corresponding to an episode).

For a concrete realisation of our RL approach, we employ the widely used Soft-actor-critic (SAC) algorithm [35, 36], an entropic-exploration based approach which has demonstrated good performance for model-free continuous control, combined with dropout Q-networks [37] to improve sample efficiency, and distributional value estimators to reduce overestimation bias [38]. A brief overview of this policy gradient actor-critic model can be found in Appendix A, and a list of hyperparameters in Appendix B.

#### 3.1 States and observations

For the purpose of quantum gate control, the agent's observation of the environment requires information about the unitary operator. We investigate the extent of information about the unitary  $U_t$  and its effect on agent performance and interpolate between providing minimal information and performing an exact tomographic reconstruction.

One choice is an observation that is constructed from the history of inputted pulses (i.e.  $o_t = \epsilon_{0:t}$ ) and represents a minimum limit of information acquired about the unitary. Since there is a non-injective mapping from pulses to a unitary operator  $\epsilon_{0:t} \mapsto U_t = U(\epsilon_{t-1})U(\epsilon_{t-2})\dots \mathbb{1}$  (this is similar to a belief state representation), we hypothesise (and test) that the agent may still be able to learn using this information. In this opposing limit, a choice of directly inputting the unitary (i.e.  $o_t = U_t$ ) into the observation represents maximal informational acquisition. This corresponds to an exact tomography of a unitary. In the intermediate regime, a choice of performing a (simulated) quantum process tomography and collecting measurement statistics yields a noisy observation and partial information about the unitary. For this latter case, we use a minimal set of positive operator-valued measures (POVMs) to reconstruct the unitary operator (Appendix C).

Additionally, since an agent has no apriori knowledge if the number of time steps and the total protocol time are fixed, we must include the time-to-go [39] in the RL observation, as it is a time-limited task.

#### 3.2 Actions

The action space is a continuous set of real values in a closed interval  $\mathcal{A} = [\epsilon_{\min}, \epsilon_{\max}]$ . The choice of a continuous action space is motivated by the desire for a fine-grained control of the pulse amplitudes. However, alternative designs may impose further constraints. For example, the action space could be a closed interval  $[-\Delta\epsilon, \Delta\epsilon]$  that changes the current pulse amplitude by the chosen value, restricting the protocol space to smoothly varying pulses [17]. For simplicity, we only use the simplest case of a continuous bounded value.

#### 3.3 Rewards

As a choice of a reward signal or figure of merit, we use a function of the negative logarithmic gate infidelity (NLIF), a simple distance measure between our generated gate and the desired gate (e.g. CNOT):

$$f = -\log_{10} \left( 1 - \left| \frac{\text{Tr} \left( U_{\text{target}}^{\dagger} U_{\text{final}} \right)}{d} \right|^2 \right)$$
 (7)

Here, a logarithmic scale is used ensuring that the agent receives a distinguishable signal even at high fidelities.

Despite its simplicity, the presence of decohering and shot noise, both of which may be present when obtaining the final gate, presents a challenge to reward functions based on the NLIF. The fidelity scales with the system noises up to a quartic term [26] while scaling exponentially with number of shots with the measurement noise (Appendix C).

We aim to identify protocols that are robust with respect to these noise sources. One approach is to constantly monitor the effects of noise on gate generation and adjust the control pulses accordingly. For this purpose, we can use a reward function of the NLIF given at the final time-step. However, more realistically, we intend to find control pulses that perform well over many noise realisations, and therefore we use a noise-averaged NLIF as a reward function. Both choices are investigated in the subsequent section.

#### 4 Results

In all cases below, we optimise for a CNOT gate, as we would like to produce accurate entangling protocols as a general requirement for useful quantum algorithms.

An RL loop consists of inputting an action  $(a_t)$ , and obtaining feedback  $(o_t, r_t)$ . In all of the scenarios below, we keep the former as a number in a continuous bounded interval. We investigate the nuances of RL agent design components with respect to the observation and reward functions, and how they affect agent performance. First,

the effects of finite rise-time are investigated (Section 4.1), followed by the effects of noise in different reward setups (Section 4.2, Section 4.3). Finally, we examine a setup with tomography statistics (Section 4.4).

Additionally, in the following experiments, we train over multiple seeds to take into account the stochasticity of neural network parameter initialisation, the randomness of RL's exploration-interaction based training, and the randomness in the cases of quantum dot system noise as well as the simulated shot noise of gate tomography. For noise-averaged fidelities (Section 4.3, Section 4.4), we take the maximum over our training realisations as we are only interested in obtaining the best possible pulses.

#### 4.1 Observations

Even in the simplest regime of no shot or system noise, the delayed response requires attention, as it presents a challenge to the Markovianity of the decision process. For unitary-only based observations, if the sampling interval  $T_s$  is shorter than the delay caused by the finite rise-time effects, the effect of the previous action is not fully accounted for, as the agent must choose another action before the full effects of previous action are realised.

A simple solution is to fix this rate so this situation is avoided. However, too few actions in a chosen protocol length can affect the controllability, impacting performance. We investigate the inclusion of the current value of the pulse amplitudes in the observation model as a method to inform the agent of the achievable bounds of its current convoluted action. This restores the Markovianity of the setup. In the case of a greater delay (i.e. greater than  $2T_s$ ), the set of  $n \geq 2$  previous pulses would be required. We test this hypothesis by comparing the agent's performance when the observation is  $o_t = (T - t, U_t)$  and  $o_t = (T - t, V_t)$ , where  $U_t$  corresponds to an exact tomography of the gate.

We use a simple reward function to measure agent performance. We use a sparse reward based on the final negative log-infidelity between the produced gate and the CNOT gate:

$$r_t = \begin{cases} f & \text{if } t = T \\ 0 & \text{otherwise} \end{cases} \tag{8}$$

For simplicity, the actual response kernel (Fig. 2 (b)) is replaced with a plain Gaussian function with a fitted standard deviation to the actual response function. We take 50 actions with a protocol length of 50ns, such that the sampling period is  $T_s = 1$ ns. We manipulate the peak position of the Gaussian to produce smaller or larger delay effects on the input pulse.

The comparative performance between the two observation models is shown in Fig. 3 (a). We see a drastic improvement of up to two orders of magnitude in the agent's performance as delay time relative to the sampling period increases. In addition to the greater reward, the stochasticity of the training is reduced, signifying a greater ease of learning, as seen in Fig. 3 (b). Including more of the pulse history may be required if the delay is greater than two actions, as this would restore the Markovian properties and allow the agent to make better informed decisions. This choice is maintained in the following sections.

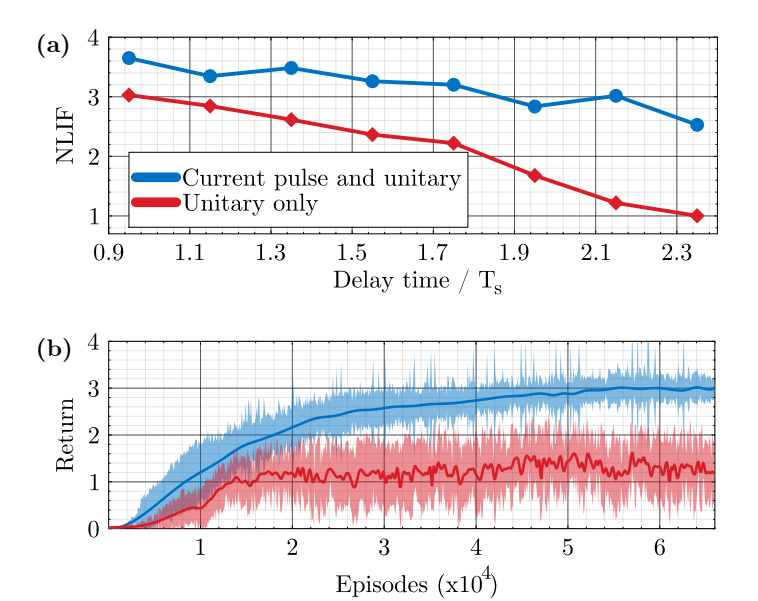


Fig. 3 (a) A plot showing the effect of the delay time (divided by the sampling period) of a convolution filter (i.e. the mean of a Gaussian kernel) with respect to the final mean NLIF (between our RL-produced gate and CNOT) obtained by an agent after training on a noise-free quantum environment (over many training seeds). In the case  $o_t = (T - t, U_t)$  ( $U_t$  is an exact tomography at each time step), we see a degradation of performance as the mean of a Gaussian kernel is shifted in time, corresponding to decrease in the Markovianity of the situation. Inclusion of the current pulse in agent's observation (i.e.  $o_t = (T - t, \epsilon_t, U_t)$ ) leads to a drastic improvement in performance. (b) The training curves (return (cumulative reward) vs. episodes) of the two choices using a kernel with a delay time of  $\sim 2.15$ ns. The agent learns superior protocols faster and with less variance over different seeds (shaded) when the extra information about the pulse is included in the observation.

#### 4.2 Noisy evolution

We will now examine the agent's performance in the full presence of all noise contributions (Eq. 6) and an observation that includes the current pulse, necessitated from the above discussion. In the presence of system noise, we simply use the noisy unitary evolution  $\tilde{U}_t$  (i.e. the unitary resulting from a particular noise realisation) as part of our agent's observation input, such that the total observation is  $o_t = (T - t, \epsilon_t, \tilde{U}_t)$ . As before, a sparse reward (Eq. 8) is employed, and we investigate agent behaviour with noisy trajectories generated by hyperfine noise on the drift and fast and slow charge noise contributions on the pulses.

We evaluate the performance of an agent across a range of total protocol lengths and number of actions (i.e. inputs to the AWG), and examine performance variability, aiming to achieve a desired performance of a fidelity of at least  $\mathcal{F} = 0.999$ .

From Fig. 4, we observe some key features. Firstly, the quantum speed limit is manifest when the total protocol length is short, resulting in poor performance across all possible number of actions. Secondly, although there are multiple regions that exceed the performance threshold, there is variability in the combination of protocol

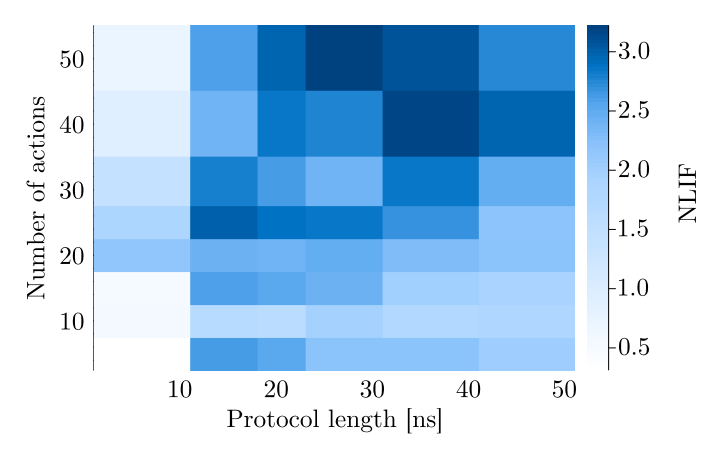


Fig. 4 A heatmap of average final negative log fidelities with varying number of actions and protocol lengths. There are some sweet spots with superior performance, but the agent achieves NLIFs of > 3 in multiple scenarios, with universally poor performance past the quantum speed limit.

length and number of actions. We identify sweetspots where fidelities are greater, with a preference for combinations involving shorter protocol lengths and a fewer actions.

One artefact of RL optimisation is its adaptability to fluctuations of the environment, a feature of the conditional distribution-based training of RL. We investigate this aspect by considering how a trained agent's protocols change in different noise realisations. As we see in Fig. 5 (a), two different noise realisations lead to minor adjustments in the agent's actions, resulting in variations in the final protocol (exchange interactions) that maintain optimal performance of  $\mathcal{F}=0.999$ . or greater. On the contrary, if the protocol was fixed, the performance over differing noise realisations may vary significantly. Additionally, Fig. 5 (b) shows the variability in performance when using the best-performing fixed protocol compared to a dynamic, noise-dependent adjusting protocol, consisting of a sequence of 20 steps and with a protocol length of 30 ns, over 100 noise realisations. The latter maintains a mean infidelity of approximately  $10^{-3}$ . An alternative strategy would be to optimise with respect to a noise-averaged reward in order to produce protocols that are performative over the different realisations. This method is employed in the next section.

We also explore how the different choices of protocol length and number of actions affect the trajectory of the separable part of the Hilbert space. We apply our CNOT gate to  $|10\rangle$  (i.e. a controlled bit flip) with two different combinations of protocol length and number of actions. In Fig. 5 (c), for a shorter protocol and fewer actions, we observe that the target qubit transitions faster towards the opposite pole of the Bloch sphere. However, it is still over-parameterised, resulting in non-geodesic behaviour. On the contrary, a longer protocol with many actions has periods of low pulses, leading to circular revolutions on the Bloch sphere. This is optimal behaviour as minimal energy is applied and the fluence (i.e. the integral over time of pulse power) is at a minimum. Indeed, as demonstrated in Fig. 5 (d), protocols that have higher mean reward at the end of training also have a lower total power. This illustrates that RL's open-box optimisation may lead to drastically different physical behaviour, including desirable secondary outcomes.

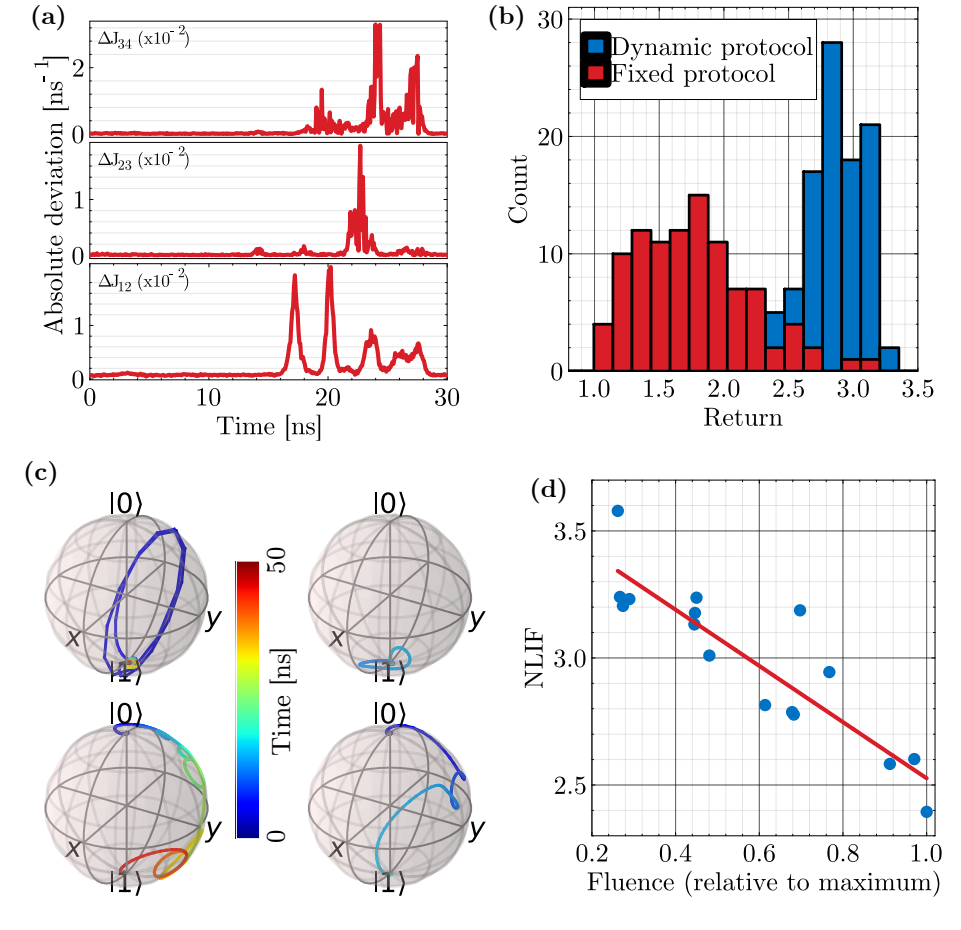


Fig. 5 (a) The absolute deviation between two different exchange interactions of post-filtered protocols, each with different noise realisations. The agent is able to learn adaptive control protocols, with different noise realisations leading to slight adjustments in the protocol to maintain performance. (b) Using the same protocol for subsequent noise realisations results in poorer performance (red), whereas using a dynamical protocol greater performance (blue). (c) Time evolution on the separable parts of the Bloch sphere for each logical qubit starting from |10⟩ for different protocol lengths and actions with (20 actions, 20 ns) (right) and (40 actions, 50 ns) (left). We see the trajectories vary demonstrating the ability of RL agents to find a diverse set of solutions. (d) The relative fluence (cumulative power of pulses) vs. the final mean reward. Pulses that produce higher fidelities also minimise the total spent energy.

#### 4.3 Noise-robust entangling strategies

For a more realistic scenario closer to a feasible experimental setup, we aim to find fixed control protocols, that are robust against fluctuations in system parameters induced by noise effects, but without the constant monitoring of noisy trajectories as in the previous section.

In this setting, the choice of observation is the time-to-go, current pulse, and a function of the simulated unitary gate in the absence of any noise. Although the true evolution of the system is noisy, this observation constitutes a belief state and corresponds to the expectation of noisy trajectory realisations. In other words, we can perform experimentally realisable closed-loop control by providing the agent with information about the expected trajectory of its actions, without direct input about the current noise realisation.

Additionally, since there is a (non-injective) mapping from the pulse history to the current unitary operator, an observation of either the gate or the pulse history can be used (i.e.  $o_t = (T - t, \epsilon_t, \epsilon_{0:t})$  or  $o_t = (T - t, \epsilon_t, U_t)$ ). We investigate the performance of the agent with respect to these two choices of observation.

To find robust protocols with respect to system noise, an averaged infidelity is used, whereby an agent optimally finds a protocol that works across many different noise realisations:

$$r_t = \begin{cases} \langle f \rangle_{N_r} = \frac{1}{N_r} \sum_{n=1}^{N_r} f_n & \text{if } t = T \\ 0 & \text{otherwise} \end{cases}$$
 (9)

Here,  $N_r$  is the number of realisations, chosen such that there is a convergence in agent performance. For each realisation, the unitary gate used in the fidelity  $f_n$  is the final noisy gate obtained using the same pulses generated by the agent, but with different system noise contributions.

In this regime, our experimental conditions are the same as for traditional noise-robust, gradient-based methods, absent of tomographic data for the unitary, which would only be performed in the final time step to calculate the fidelity. Consequently, the resulting performance can be suitably compared with previous results. Cerfontaine *et al.* [26] reported a fidelity past the threshold of 99.9% using their gradient-based approach mentioned mentioned in Section 2. We use their method as implemented in the qopt library [40] as a competitive benchmark.

We note that the fidelities reported below lie lower than said reference, indicating that the two models are not exactly equivalent. Further analysis revealed, that slightly adjusted sample periods render comparable reachable fidelities, as we will discuss towards the end of this section. We optimised over a set of protocol lengths and number of actions in both approaches.

Fig. 6 (a) shows that the agent can learn to an NLIF of about 1.8 in this regime with full observation of the noise-free unitary at all but terminal time steps and to an NLIF of about 1.5 with just the pulse history, which requires significantly less information. In the former case, the performance is similar to our qopt simulation (that only consists of drift noise). The protocol duration in this setting is 20 ns and consists of 30 actions.

However, we note that this performance does not appear to stem from limitations of RL training with system noise. First, we simplify the RL environment to a simple one-qubit quantum system, with one control (and exchange interaction) and drift term, and only use the drift noise as it is the dominating terms for the infidelity at this sampling period. In Appendix D, we show that, as we scale the noise, both RL and qopt fidelities scale equivalently. Therefore there may be a fundamental upper

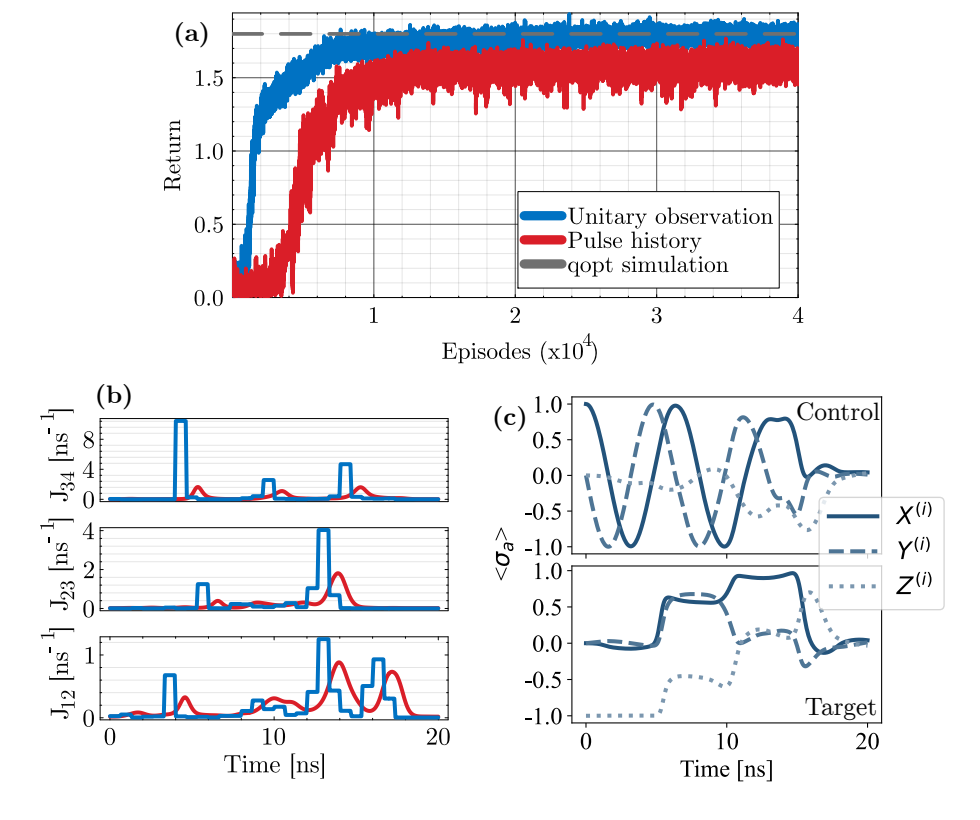


Fig. 6 (a) The training curves for an RL agent with a robust reward consisting of maximum negative log infidelities. The RL agent will perform marginally better if it has full access to the current unitary gate at time step t compared to only having the history of actions (with which a non-injective mapping to a unitary can be constructed). The former has a similar performance to our gradient based-simulation using qopt (only consisting of the drift noise term). (b) A full protocol of a robust pulse of 20 ns with 30 actions. In blue are the actions corresponding to the discretised pulses inputted to the AWG device and the red lines are the smoothed pulses affected by the finite response of the qubit. (c) The expectation values of the logical qubits for an entangling operation on  $|0+\rangle$  with respect to time. The logical qubit (below) is entangled in steps with a sequence of rotations on the physical qubits.

bound on the averaged fidelity with noisy time evolution. Likewise, training curves yield similar infidelity limits that match qopt.

A typical obtained protocol (Fig. 6 (b)) has hard kicks in the input signals or actions, causing weaker smoothened signals that affect the exchange interactions between the four dots. First, the two logical qubits are rotated locally by  $J_{12}$  and  $J_{34}$ , such that they can be suitably entangled by  $J_{23}$ , and then they are rotated back to the original basis. This can also be seen in the expectation values of each Pauli operator on each logical qubit in Fig. 6 (c), when starting with an initial state of  $|+0\rangle$ , which allows for entanglement.

To investigate the effect of different noise contributions based on the sampling periods  $T_s$ , we examine the scaling of the individual noise contributions by adjusting the time and energy scales (reciprocally, thus keeping the overall evolution duration

fixed) of the system but reuse the same obtained protocol without re-optimisation [26]. We then plot the infidelity change of individual noise contributions (i.e. the others are switched off) as well as the overall noise with respect to the scaling of the sample period (i.e.  $k/T_s$  where k is the scale factor) (Fig. 7 (a)). We observe that regions of long sample periods (and therefore less frequent qubit manipulation) are heavily affected by qubit drift or hyperfine noise. At lower sampling periods, we see a negligible rise in the noise contributions of the fast time-correlated charge noise, and it is expected to further scale with respect to the power  $\alpha$ , but is otherwise suppressed by the overall scale. We conclude that choosing a higher sampling rate by an order of magnitude may be prudent to get the most out of agent performance. To confirm this, we train an agent from scratch at a scale factor of  $100/T_s$  and observe that its performance surpasses the expected baseline from the sampling period scaling.

In addition, we also evaluate the robustness of our protocol as we increase the relative noise strengths in Fig. 7 (b). While the fast charge noise is dominated mostly by the time scale and therefore suppressed, the hyperfine and slow charge noise scales exponentially past the initial baseline value, which we can see by the linear relation in the log-log plot.

#### 4.4 Process Tomography

Finally, for the most complex case, we slightly modify the previous setup to make it as close as possible to a feasible experimental setup. For the calculation of fidelity, our obtained unitary is estimated using limited or partial tomography and its associated measurement statistics and shot noise. We investigate the effects between taking a small and a large number of measurements on agent performance due to this added uncertainty. In other words, we explore whether shot noise causes confusion to the agent.

To this end, we take the following approach: First, using a fixed pulse generated by the agent, we obtain a unitary after an evolution with a system noise realisation. Then, we perform a single-shot measurement of this unitary by selecting a random input quantum state, as process tomography requires a suitable set of state tomography experiments, as well as a random POVM element (Appendix C). We then measure the outcome of this combination of POVM element and input state and only one data point is collected per system noise realisation. We repeat this process for  $N_m$  runs (i.e. we collect  $N_m$  snapshots). Using the collected measurement statistics, we then reconstruct a unitary which includes the statistics of both system and shot noise. This unitary is then used for calculating the fidelity, and hence the reward.

However, due to the high computational cost of our experiments, due to performing a large number of snapshots multiplied by the requirement of training over many episodes, we also apply an alternative approach. We revert to the setup in the previous section, but for each unitary generated by a realisation of system noise, we add an additional additive Gaussian noise. In other words, we model the shot noise using a Gaussian with a chosen standard deviation:

$$r_T = \langle f(\text{CNOT}, U_T + \delta U) \rangle_{\delta U \sim \mathcal{N}(\mathbf{0}, \sigma^2 \mathbb{1})}$$
(10)

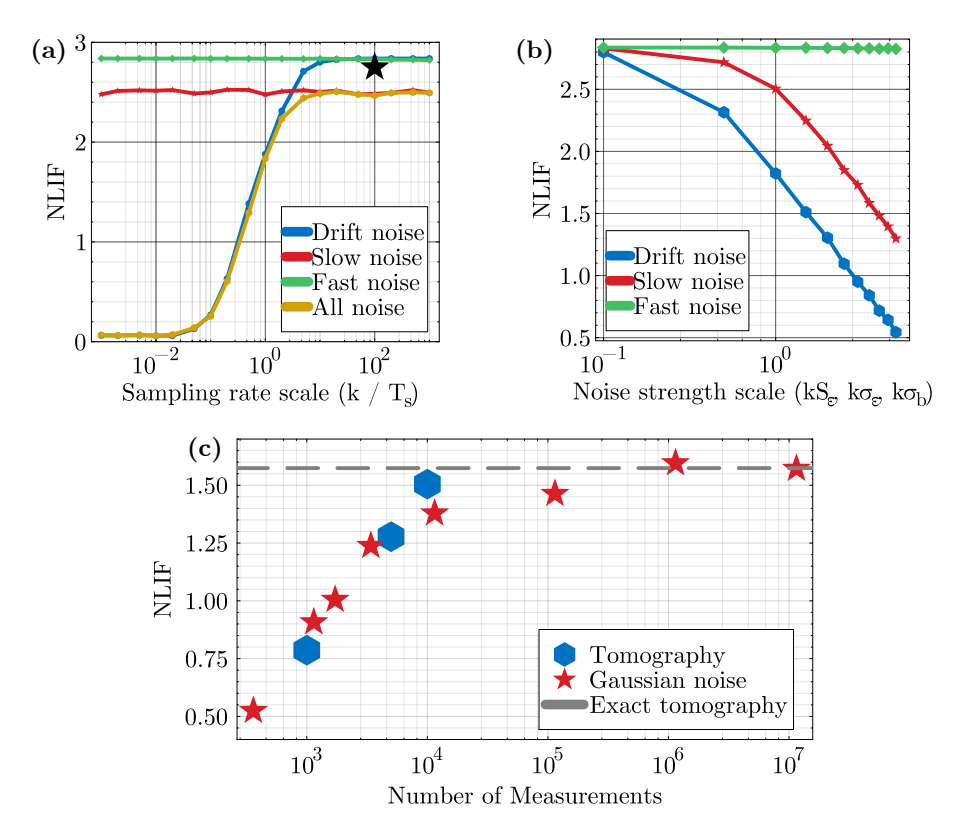


Fig. 7 (a) The infidelity scaling of the noise contributions with respect to the frequency rate (i.e.  $k/T_s$  for scale factor k) without reoptimisation. We observe that the hyperfine noise contributions dominate in low frequency scales, whilst the slow charge noise is independent. The overall factor of the fast charge noise makes this noise contribution negligible. The black star is the fidelity achieved from a newly trained agent trained from scratch at a scale of 100. We observe that its performance surpasses the expected baseline. (b) Infidelity scaling with respect to the noise scale (i.e.  $k(S_{\epsilon}|\sigma_{\epsilon}|\sigma_{b})$ ). While the fast charge noise is dominated mostly by the time scale and therefore suppressed, the hyperfine and slow charge noise scales exponentially. In other words, small increases in the noise strengths have negligible effect on agent performance. (c) Negative log-infidelity as a function of the number of measurements per episode used to perform process tomography. In circles are unitaries reconstructed by POVM-based multinomial statistics, while the stars represent an approximation using additive Gaussian noise with a standard deviation scaled to match the expected number of measurements to reach the same infidelity with POVM-tomography (Appendix C). The final NLIF converges to the exact tomographic performance as the number of measurements becomes large.

Here,  $U_T$  is a noisy realisation of the generated unitary and we add to it a  $d \times d$  noisy matrix, representing the shot noise.

To ensure the accuracy between the previous POVM-based approach and our alternative simulated measurement noise, we match the infidelity scaling (of only the shot noise and ignoring the system noise) of the additive Gaussian noise with standard deviation  $\sigma$  with the infidelity scaling of a POVM-based approach using a certain number of snapshots. In other words, we can crudely approximate the number of snapshots N to a standard deviation or noise scale (Appendix C).

In Fig. 7 (c), we observe the effect of the number of snapshots per episode on the final NLIF in a regime consisting of 30 actions and a protocol length of 30 ns. There is a near order-of-magnitude gain of performance as the number of snapshots per episode increases, converging to the exact tomographic result based on the previous subsection. Notably, by taking just 1000 snapshots, the agent converges to an NLIF of approximately 0.8. However, this result is not due to limitations in agent learning, but rather the fidelity bound of an estimated unitary gate with 1000 snapshots, as can be seen in Appendix C. Furthermore, the tomographic data matches the alternative Gaussian approach for a smaller number of measurements, such that we can reliably infer the expected tomographic performance in the large measurement limit without the computational constraints. Consequently, our experimentally realistic protocol is constrained by the desired fidelity threshold, which may be bounded by the shot noise if insufficient measurements are performed, but is ultimately limited by the system noise. In other words, shot noise does not lead to additional confusion in agent learning.

## 5 Conclusion

We investigated the feasibility of using RL to control realistically modelled quantum hardware, subject to three major constraints: rise-time effects, multiple noise contributions to the system (including time-correlated noise), and limited information about the realised unitary via simulated tomography in the presence of the aforementioned system noise. We sequentially added each constraint to test RL-agent performance in the face of increasing complexity.

Firstly, we demonstrated that proper and carefully considered agent design is necessary to achieve satisfactory performance, even if seemingly trivial. Small changes in RL state observation had drastic effects on the final gate fidelities achieved, as the finite rise-time effects of controlling hardware broke the Markovian properties required needed for successful learning. Including pulse information in the observation restored these properties.

Secondly, we introduced decohering noise to the quantum system, but allowed the agent to observe deviations in the unitary trajectory. We achieved a performance of 99.9% fidelity for certain combinations of protocol lengths and number of agent actions. Additionally, in this setting, the agent varies its inputs slightly to correct for the noise to maintain an optimal performance. Furthermore, optimal pulses were found to minimise the total power as a nascent outcome.

Thirdly, we matched or surpassed the baseline performance of our alternative, gradient-based approach in similar regimes by using a noise-averaged reward to find a single noise-robust pulse. Furthermore, given only information about the protocol (i.e. sequence of pulses), an agent is able to infer a mapping onto a unitary and perform close to the baseline without direct information of the unitary (sans a final fidelity reward function), and is subsequently free of any model-bias.

Finally, we performed a simulated process tomography on the generated unitary to calculate the fidelity. This meant that the agent had to learn in the presence of both system and measurement noise. Despite the additional shot noise, we found that the agent performance was constrained by the number of measurements that matched the

fidelity of quantum process tomography alone. In other words, with enough measurements, achieved fidelities were only limited by the system noise and shot noise did not contribute to a greater confusion in learning.

Two avenues would be of interest for future research, independent of the specific caveats of RL control of quantum dots. On the side of RL design, it would be interesting to investigate the effect of incorporating autoregressive neural network structures to augment agent capabilities, particularly when only minimal information is available, such as with pulse-only observation data provided to the agent.

Another avenue of interest would be to investigate incorporating RL into existing frameworks. One advantage of using RL with a noise-averaged fidelity as a reward function is that this training can be used as a form of offline pre-training with a known Hamiltonian (and noise) model. Consequently, once a simulated, noise-averaged baseline has been established, it is possible to further optimise the protocol with respect to real-device noise. This additionally avoids the inference overhead of neural networks, with an alternating closed-loop sequence of many runs and their respective fidelities and a RL-training step to maintain or improve noise-robust pulses. This pre-training stage could easily be replaced with existing gradient-based or model-aware methods, with RL being used to improve them yet remaining general enough to train from scratch.

## Acknowledgements and data availability

We thank Max Oberländer for helping us with using the qopt package developed at PGI-11 and Hendrik Bluhm for helpful comments on the manuscript. This work was supported through the Helmholtz Initiative and Networking Fund, Grant No. VH-NG-1711.

The code used for this paper was made by the authors in the Julia programming language [41] and is in active development at <a href="https://github.com/EmergentSpaceTime/RLQuantumControl">https://github.com/EmergentSpaceTime/RLQuantumControl</a>. The RL generated data which was used for this paper as well as the scripts to generate the plots can be found at 10.5281/zenodo.16900638.

## A Reinforcement Learning

Readers interested in an in-depth description of reinforcement learning are referred to Ref. [8]. The following is a brief overview of the main concepts. Reinforcement learning (RL) is built around three primary components: observation, decision-making, and feedback. The central framework uniting these aspects are *MDPs*.

**Definition.** A Markov decision process (MDP) is the tuple  $(S, A, T, R, \gamma)$  where:

- S is a set of states
- $\mathcal{A}$  is a set of actions
- $\mathcal{T}: \mathcal{S} \times \mathcal{S} \times \mathcal{A} \longrightarrow [0,1]$  is the state-transition probability:  $T^a_{ss'} = \mathbb{P}\left[s_{t+1} = s' | s_t = s, a_t = a\right]$

- $\mathcal{R}: \mathcal{S} \times \mathcal{A} \longrightarrow \mathbb{R}$  is the reward function:
  - $r_s^a = \mathbb{E}[r_{t+1}|s_t = s, a_t = a]$
- $\gamma \in [0,1]$  is the discount factor

An MDP has the Markovian property of independence from past and future states.

Additionally, to formalise decision-making, we must define a policy.

**Definition.** A **policy**  $(\pi)$  is a conditional probability distribution over the set of actions  $\mathcal{A}$  and the set of states  $\mathcal{S}$ , denoted  $\pi(a|s)$ .

A set of states,  $\mathcal{S}$ , represents the possible configurations of an *environment*. An environment can be anything from a chess game to a model of urban traffic. An *agent* is an abstract object that performs an *action* from a set of possible actions,  $\mathcal{A}$ , which affect the state of the environment. Once an action is performed, the state of the environment transitions to another possible state via a conditional probability function. For example, going from any one chess configuration to another may not be possible. In other words, the transition function models the dynamics of the environment.

Decision-making cannot be informed by states and actions alone. To achieve this, an objective or goal is required. Such an objective is modelled with a *reward*, enabling the possibility of optimisation or improvement. To model an agent's choice of action or its decision-making a policy is used. The goal of RL is to find a optimal policy  $\pi^*$  that maximizes the cumulative reward:

**Definition.** The (discounted) return  $G_t$  is the cumulative reward obtained starting from the time step t:

$$G_t = \sum_{k=0}^{\infty} \gamma^k r_{t+k+1} \tag{11}$$

A policy is evaluated through the following function:

**Definition.** The action-value function or q-function is the expected return starting from a state s, taking taking an action a, then following a policy  $\pi$ :

$$q_{\pi}(s, a) = \mathbb{E}_{\pi}[G_t|s_t = s, a_t = a]$$
 (12)

These q-functions have the following optimality condition:

$$q_{\pi}^{\star} = \max_{\pi} q_{\pi}(s, a) \tag{13}$$

The optimal policy is not unique, but its q-function is. We can use the recursive nature of the above equations to find an optimal solution via dynamic programming, giving the Bellman equation:

$$q_{\pi}^{\star}(s, a) = r_s^a + \gamma \sum_{s' \in \mathcal{S}} T_{ss'}^a \max_{a'} q^{\star}(s', a')$$
 (14)

Two important challenges arise from using tabular methods (i.e. keeping a memory of all combinations of state and actions to calculate the q-function). Firstly, many MDPs have state and actions spaces that are intractable. For example, the game of Go has  $10^{170}$  configurations. Furthermore, MDPs with continuous states and actions cannot be modelled. Secondly, in Eq. 14, we explicitly need the dynamics of the system via the transition probabilities, which are often either unavailable or intractable, as previously aformentioned.

For the first problem, since the state and action spaces of many control problems, including quantum control, are continuous or involve vast state spaces, we parameterise our Q-functions and policies using neural networks. They satisfy the universal function approximation theorem [42], therefore can approximate any function up to local convergence. This allows us to construct a function mapping continuous or discrete state and actions to a q-value or policy probability distribution.

For the second problem, we employ temporal-difference (TD) learning. This approach involves maintaining an improving estimate of the q-function. Learning is combined with gaining experience, as this action-value-estimate is updated in an online fashion. Initially, after each time step, we calculate a target towards which we move our current q-estimate. This target itself is an estimate of the current q-function. In other words, we update a guess towards a guess. From the recursive nature of the Bellman equation, we aim to converge to the true q-function by minimising the following error:

$$\delta_t := r_{t+1} + \gamma \max_a q(s_{t+1}, a) - q(s_t, a_t)$$
(15)

Combining the two solutions, we employ actor-critic style methods (Fig. 8), simultaneously optimising parameterised policies and parameterised q-functions using gradient descent methods such as ADAM [43]. An actor is nothing more than a parameterised policy, which takes a state and outputs a conditional distribution of possible actions. A critic is a parameterised q-function which takes a state-action pair and outputs a number.

In addition, we employ a chosen algorithmic variation of actor-critic known as soft actor-critic [35, 36]. Here, we augment the reward with the current policy entropy to encourage exploration:

$$r_t' = r(s_t, a_t) + \alpha H(\pi_\theta(\cdot|s_t)) \tag{16}$$

A controlled temperature parameter,  $\alpha$ , is used to interpolate between high and low exploratory behaviour. The recursive Bellman update becomes:

$$Q_{\phi}(s_{t}, a_{t}) = r_{t} + \gamma Q_{\phi}(s_{t+1}, a_{\text{new}}(s_{t+1})) - \alpha \log \pi_{\theta}(a_{\text{new}}(s_{t+1})|s_{t+1})$$
(17)

Here,  $a_{\text{new}}(s_{t+1}) \sim \pi_{\theta}(\cdot|s_{t+1})$ . The q-network is then trained to minimise this modified temporal difference leading to (after some algebraic manipulation), a cost function for the q-network:

$$J_{\phi} = \frac{1}{|\mathcal{B}|} \sum_{\tau \sim \mathcal{B}} \left( Q_{\phi}(s, a) - \delta(s, r') \right)^2 \tag{18}$$

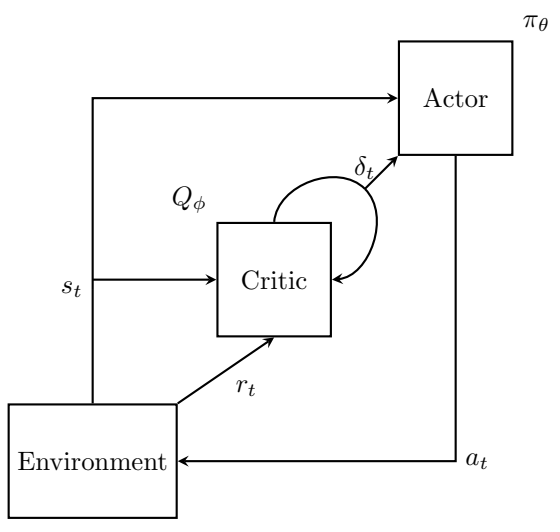


Fig. 8 A general overview of actor-critic methods in RL. The critic (i.e. a parameterised q-function) judges the actor (i.e. a parameterised policy) and gives feedback whilst simultaneously improving its estimation using the temporal difference error  $\delta_t$  (Eq. 15).

Here,  $\delta(r, s')$  is defined to be:

$$\delta(r, s') = r + \gamma \left( Q_{\phi}(s', a_{\text{new}}(s')) - \alpha \log \pi_{\theta}(a_{\text{new}}(s')|s') \right)$$
(19)

Here,  $\mathcal{B}$  refers to batches of sampled experience trajectories, with  $\tau = (s, a, s', r)$ . The policy cost function is to maximise the expected return:

$$J_{\pi}(\theta) = \underset{\tau \sim \pi}{\mathbb{E}} \left[ G(\tau) \right] \tag{20}$$

Since the rewards are estimated using the q-function, we can rewrite this as:

$$J_{\theta} = \frac{1}{|\mathcal{B}|} \sum_{\tau \sim \mathcal{B}} \left[ -\alpha \log \pi_{\theta}(\tilde{a}_{\theta}(s)|s) + Q(\tilde{a}_{\theta}(s), s) \right]$$
 (21)

Note that the policy loss requires sampling new actions  $a_{\theta}(s) \sim \pi(\cdot|s)$ , which are obtained using the reparametrisation trick [44] in order to compute gradients.

Further enhancements to SAC include using a distribution of critics and taking the minimum of the q-values to reduce overestimation bias [38]. Furthermore, the q-networks may be augmented with dropout layers that have empirically demonstrated improving sample efficiency [37].

Finally, an important aspect of MDPs must be mentioned. In this appendix<sup>2</sup>, we have interchangeably used the terminology of states and observations. For some environments such as the full-information games Chess and Go, these notions are equivalent. However, many environments prevent access to state information. For

<sup>&</sup>lt;sup>2</sup>And other parts of this paper.

example, in many video games, information about the state is typically limited to audio-visual data, as underlying parameters are hidden from the agent. Likewise, quantum systems fundamentally limit accessible information about a quantum state. To distinguish this facet of MDPs, we define the following:

**Definition.** A partially observable Markov decision process (POMDP) is the tuple

 $(S, A, O, T, R, B, \gamma)$  where:

- S is a set of states
- $\mathcal{A}$  is a set of actions
- $\mathcal{O}$  is a set of observations
- $\mathcal{T}: \mathcal{S} \times \mathcal{S} \times \mathcal{A} \longrightarrow [0,1]$  is the state-transition probability:  $T^a_{ss'} = \mathbb{P}\left[s_{t+1} = s' | s_t = s, a_t = a\right]$
- $\mathcal{R}: \mathcal{S} \times \mathcal{A} \longrightarrow \mathbb{R}$  is a reward function:

 $R_s^a = \mathbb{E}[r_{t+1}|s_t = s, a_t = a]$ 

•  $\mathcal{M}: \mathcal{S} \longrightarrow \mathcal{O}$  is the observation function:

$$\mathcal{M}_{so} = \mathbb{P}\left[o_t = o \middle| s_t = s\right]$$

•  $\gamma \in [0,1]$  is the discount factor

A POMDP has the Markovian property of independence from past and future states.

The (stochastic) observation function adds uncertainty to an agents decision-making, as it now needs to additionally learn a model distribution over the states:

**Definition.** The **belief state** is a probability distribution over the states given a **history**  $h_t = (o_{0:t}, a_{0:t-1})$ :

$$b_t(s_t) = \mathbb{P}\left[s_t = s | h_t\right]$$

The mapping from a history to the corresponding belief is given by a function:

$$f^*(h_t) = b_t$$

Such a belief is a sufficient statistic of the history (a compact summary of the history). It's update function can be calculated recursively from an initial observation:

$$b'(s') = \frac{\mathcal{M}_{s'o'} \sum_{s \in \mathcal{S}} \mathcal{T}^a_{ss'} b(s)}{Z}$$

Here, Z is the normalisation factor. We obtain an update equation:

$$b' = f(b \mid a, o')$$

## B Reinforcement Learning Hyperparameters

The learning rate, discount parameter (Appendix A), and mini-batch size were chosen similar to Haarnoja et al. [36] and were tested and confirmed to be performative

through a series of ablations. The experience replay capacity (i.e. the number of stored experiences) was reduced from 1M to 100K as this smaller buffer did not alter performance. Likewise, the number of outputs and top outputs for the Q-networks is matched with [38], and the dropout is matched with [37]. These dropout and normalising layers help with agent stability and efficiency in training. A maximal and minimal log-variance is enforced to ensure training stability while also preventing convergence to a Dirac delta distribution. The Polyak parameter,  $\rho$ , prevents large changes in the critics distribution and is chosen to be sufficiently small to stabilise training.

RL Parameter	Symbol	Value
Discount parameter	$\gamma$	0.99
Polyak averaging parameter	$\rho$	0.005
Number of outputs for Q-networks	$q_k$	46
Number of top outputs used for TQC	$q_n$	25
Learning rate	$\eta$	5e-4
Dropout probability	p	0.01
Mini-batch size	_	256
Maximal log variance for policy	$\log  u_{ m min}$	-15
Maximal log variance for policy	$\log \nu_{ m max}$	4
Hidden layers	_	[512, 512]
Relay capacity	_	100,000

**Table 2** The parameters used for the reinforcement learning algorithm.

# C Unitary tomography

Quantum process tomography (QPT) is a method of estimating and reconstructing a process (e.g. gates) from a collection of measurements on a quantum system. Process tomography poses a greater challenge than quantum state tomography (QST) (i.e. estimating a state), as multiple inputs are needed to fully and uniquely characterise a process. A general map has  $d^2(d^2-1)$  independent parameters, as it requires  $d^2$  probe states to characterise a map  $\rho_n^{\text{out}} = \mathcal{P}(\rho_n^{\text{in}})$ , which has  $d^2-1$  independent parameters.

Unitary gate tomography exploits the symmetries of U(n) to estimate  $d^2+d$  parameters of a unitary gate. This is achieved by utilising a specific set of informationally complete POVMs and input elements [45]. Flammia *et al.* [46] show that the following set of 2d POVMs is informationally complete for pure states:

$$E_{0} = a|0\rangle\langle 0|$$

$$E_{j} = b(1+|j\rangle\langle 0|+|0\rangle\langle j|) \qquad j = 1, \dots, d-1$$

$$\widetilde{E}_{j} = b(1+i|j\rangle\langle 0|-i|0\rangle\langle j|) \qquad j = 1, \dots, d-1$$

$$E_{2d} = 1 - E_{0} - \sum_{j=1}^{d-1} E_{j} + \widetilde{E}_{j}$$

$$(22)$$

Here, a, b > 0 are chosen such that  $E_{2d} > 0$ . The input states must be chosen to account for the relative phases of the unitary elements. A suitable choice is [45]:

$$|\psi_0\rangle = |0\rangle$$

$$|\psi_n\rangle = \frac{1}{\sqrt{2}} (|0\rangle + |n\rangle) \qquad n = 1, \dots, d-1$$
(23)

The procedure for unitary tomography is as follows: Let U act on  $|\psi_0\rangle$  and perform QST on  $|u_0\rangle = U |\psi_0\rangle$  to characterise it. This involves finding the coefficients of the state, i.e.  $|u_0\rangle = \sum_k c_{0,k} |k\rangle$ . Repeat for  $|u_1\rangle$  and use the relation  $U |\psi_1\rangle \langle \psi_1| U^{\dagger} |u_0\rangle = \frac{1}{2} (|u_0\rangle + |u_1\rangle)$  to characterise  $|u_1\rangle$ , including the relative phase to  $|u_0\rangle$ . Repeat for all the inputs.

To simulate a tomography experiment, we first extract the probabilities from an obtained unitary:

$$p_{n,j} = \text{Tr}\left(U\rho_n U^{\dagger} E_j\right) \tag{24}$$

As an example, we have:

$$p_{0,0} = \langle u_0 | E_0 | u_0 \rangle = a | c_{0,0} |^2$$

$$p_{0,j} = \langle u_0 | E_j | u_0 \rangle = b \left( 1 + 2c_{0,0} \operatorname{Re} \left( c_{0,j} \right) \right)$$

$$\widetilde{p}_{0,j} = \langle u_0 | \widetilde{E}_j | u_0 \rangle = b \left( 1 + 2c_{0,0} \operatorname{Im} \left( c_{0,j} \right) \right)$$
(25)

Note that this procedure fails for  $c_{0,0} = 0$ . Then, we perform a multinomial sampling of  $N_m$  shots along d-1 input axes. This number bounds the precision of the fidelity. Finally, we reconstruct the unitary from our obtained samples using an inversion of Eq. 24 with an approximated  $p_{n,j}$ . Additionally, we map the reconstruction to the closest unitary in order to account for sampling size effects, i.e. when  $N_m$  is small, the estimated gate is not unitary.

Due to the exponential scaling of the infidelity between the actual gate and its estimated reconstruction with respect to the number of POVM measurements (Fig. 9), it is challenging to reach a desired infidelity threshold. For example,  $10^5$  measurements are required to reach an infidelity of  $10^{-3}$ , hence is both computationally expensive if simulated and experimentally costly if performed. As a result, we devise an alternative approach that is less computationally costly.

We add element-wise Gaussian noise of a certain standard deviation to the actual gate to approximate the shot noise of a POVM-based estimation. As before, we map the noisy unitary to the closest unitary to account for sampling size effects. By calculating the mean infidelity for a given a standard deviation, we extrapolate an infidelity scaling. Combined with the POVM-based infidelity scaling, we map a standard deviation to the approximate number of measurements required to achieve the same infidelity (Fig. 9). Therefore, the computationally expensive limit of a large number of measurements is approximated with a cheaper additive Gaussian noise of low standard deviation.

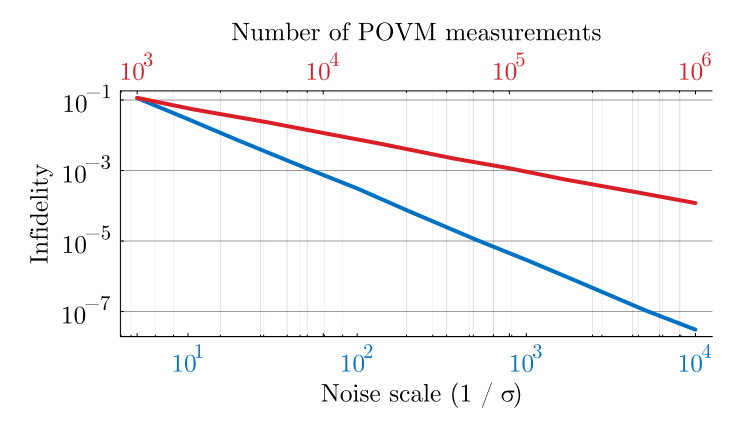


**Fig. 9** The infidelity scaling of a random 6d unitary using a POVM-based approach (red) and a simple additive Gaussian noise (blue). We use a linear fit to heuristically approximate the number of shots to the (inverse) standard deviation that achieves the same infidelity.

## D Single qubit noise-robust phase gate

We use a noise-averaged reward with exact tomography as in Section 4.3 for a simple one-qubit quantum dot system that only consists of hyperfine noise. Similar to the more complicated two-qubit case, we see in Fig. 10 (a) that we obtain a final fidelity less than the desired 99.9%, with an achieved log-infidelity of about 2.1. However, like the two-qubits, our gradient-based qopt simulation has a similar performance, additionally indicating a fidelity limit that is bounded by the noise scale and not on agent limitations, as can be seen in Fig. 10 (b), where train an RL agent and perform a qopt simulation at different noise scales.

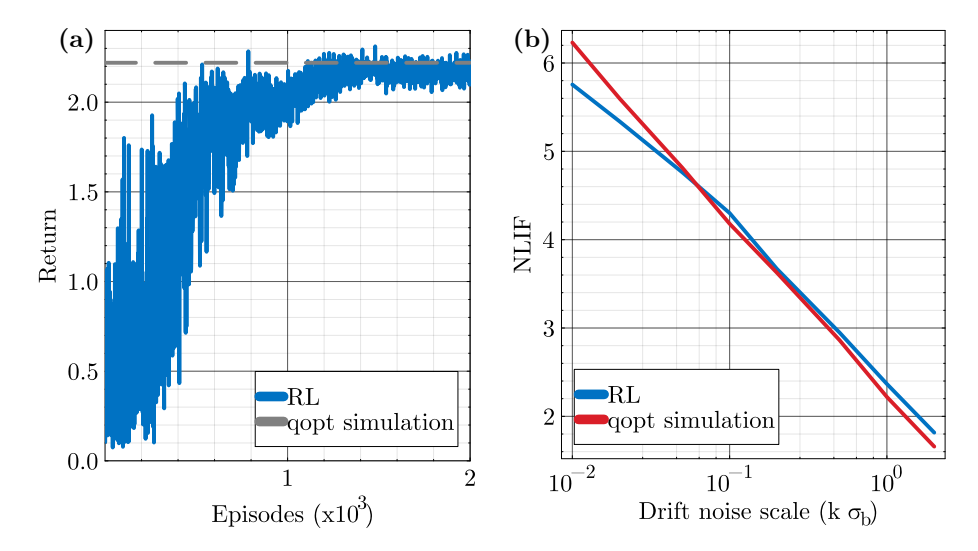


Fig. 10 (a) Final infidelity performance of both an RL agent and a qopt based simulation with respect to the drift noise scale on a simple 1-qubit system. The performance scaling indicates RL is only bounded by a fundamental infidelity scaling due to the noise and not any optimisation issues. (b) The maximum training curves for an RL agent in a 1-qubit environment with only drift noise and with a noise-averaged reward of negative log infidelities. The RL agent will perform similarly with "full" observation (i.e. exact tomography) to gradient-based approach (of a protocol length of 10ns and 20 inputs) using the qopt package.

## References

- [1] Butkovskii A, Samoilenko YI. Control of quantum systems. Automation and Remote Control. 1979;40(4):485–502.
- [2] Butkovskii A, Samoilenko YI. Control of Quantum Systems 2. Automation and Remote Control. 1979;40(5):629–645.
- [3] Glaser SJ, Boscain U, Calarco T, Koch CP, Köckenberger W, Kosloff R, et al. Training Schrödinger's cat: Quantum optimal control: Strategic report on current status, visions and goals for research in Europe. The European Physical Journal D. 2015;69(12):279.
- [4] Khaneja N, Reiss T, Kehlet C, Schulte-Herbrüggen T, Glaser SJ. Optimal control of coupled spin dynamics: design of NMR pulse sequences by gradient ascent algorithms. Journal of magnetic resonance. 2005;172(2):296–305.
- [5] de Fouquieres P, Schirmer SG, Glaser SJ, Kuprov I. Second order gradient ascent pulse engineering. Journal of Magnetic Resonance. 2011;212(2):412–417.
- [6] Krotov V. Global methods in optimal control theory. vol. 195. CRC Press; 1995.

- [7] Machnes S, Assémat E, Tannor DJ, Wilhelm FK. Gradient optimization of analytic controls: the route to high accuracy quantum optimal control. arXiv preprint arXiv:150704261. 2015;.
- [8] Sutton RS, Barto AG. Reinforcement learning: An introduction. MIT press; 2018.
- [9] Kiran BR, Sobh I, Talpaert V, Mannion P, Sallab AAA, Yogamani S, et al.: Deep Reinforcement Learning for Autonomous Driving: A Survey.
- [10] Smith L, Kostrikov I, Levine S.: A Walk in the Park: Learning to Walk in 20 Minutes With Model-Free Reinforcement Learning.
- [11] Ouyang L, Wu J, Jiang X, Almeida D, Wainwright CL, Mishkin P, et al.: Training language models to follow instructions with human feedback.
- [12] Schrittwieser J, Antonoglou I, Hubert T, Simonyan K, Sifre L, Schmitt S, et al. Mastering Atari, Go, chess and shogi by planning with a learned model. Nature. 2020;588(7839):604–609. https://doi.org/10.1038/s41586-020-03051-4.
- [13] Tsubouchi M, Momose T. Rovibrational wave-packet manipulation using shaped midinfrared femtosecond pulses toward quantum computation: Optimization of pulse shape by a genetic algorithm. Physical Review A. 2008;77(5):052326.
- [14] Dong D, Xing X, Ma H, Chen C, Liu Z, Rabitz H. Learning-Based Quantum Robust Control: Algorithm, Applications, and Experiments. IEEE Transactions on Cybernetics. 2020;50(8):3581–3593. https://doi.org/10.1109/TCYB. 2019.2921424.
- [15] Baum Y, Amico M, Howell S, Hush M, Liuzzi M, Mundada P, et al. Experimental Deep Reinforcement Learning for Error-Robust Gate-Set Design on a Superconducting Quantum Computer. PRX Quantum. 2021 Nov;2:040324. https://doi.org/10.1103/PRXQuantum.2.040324.
- [16] Niu MY, Boixo S, Smelyanskiy VN, Neven H. Universal quantum control through deep reinforcement learning. npj Quantum Information. 2019;5(1):33.
- [17] Nguyen HN, Motzoi F, Metcalf M, Whaley KB, Bukov M, Schmitt M. Reinforcement learning pulses for transmon qubit entangling gates. Machine Learning: Science and Technology. 2024;5(2):025066.
- [18] Shindi O, Yu Q, Girdhar P, Dong D. Model-Free Quantum Gate Design and Calibration Using Deep Reinforcement Learning. IEEE Transactions on Artificial Intelligence. 2024;5(1):346–357. https://doi.org/10.1109/TAI.2023.3243187.
- [19] Bukov M, Day AG, Sels D, Weinberg P, Polkovnikov A, Mehta P. Reinforcement learning in different phases of quantum control. Physical Review X. 2018;8(3):031086.

- [20] An Z, Zhou D. Deep reinforcement learning for quantum gate control. Europhysics Letters. 2019;126(6):60002.
- [21] Sivak V, Eickbusch A, Liu H, Royer B, Tsioutsios I, Devoret M. Model-free quantum control with reinforcement learning. Physical Review X. 2022;12(1):011059.
- [22] Torlai G, Wood CJ, Acharya A, Carleo G, Carrasquilla J, Aolita L. Quantum process tomography with unsupervised learning and tensor networks. Nature Communications. 2023;14(1):2858.
- [23] Sarma B, Hartmann MJ. Designing fast quantum gates using optimal control with a reinforcement-learning ansatz. Physical Review Applied. 2025;23(1):014015.
- [24] Burkard G, Ladd TD, Pan A, Nichol JM, Petta JR. Semiconductor spin qubits. Rev Mod Phys. 2023 Jun;95:025003. https://doi.org/10.1103/RevModPhys.95.025003.
- [25] Cerfontaine P. High-fidelity single- and two-qubit gates for two-electron spin qubits [Dissertation]. RWTH Aachen University. Aachen; 2019. Veröffentlicht auf dem Publikationsserver der RWTH Aachen University, Dissertation, RWTH Aachen University, 2019. Available from: https://publications.rwth-aachen.de/ record/768380.
- [26] Cerfontaine P, Otten R, Wolfe MA, Bethke P, Bluhm H. High-fidelity gate set for exchange-coupled singlet-triplet qubits. Physical Review B. 2020;101(15). https://doi.org/10.1103/physrevb.101.155311.
- [27] Muhonen JT, Dehollain JP, Laucht A, Hudson FE, Kalra R, Sekiguchi T, et al. Storing quantum information for 30 seconds in a nanoelectronic device. Nature nanotechnology. 2014;9(12):986–991.
- [28] Dial OE, Shulman MD, Harvey SP, Bluhm H, Umansky V, Yacoby A. Charge Noise Spectroscopy Using Coherent Exchange Oscillations in a Singlet-Triplet Qubit. Phys Rev Lett. 2013 Apr;110:146804. https://doi.org/10.1103/ PhysRevLett.110.146804.
- [29] Yoneda J, Takeda K, Otsuka T, Nakajima T, Delbecq MR, Allison G, et al. A quantum-dot spin qubit with coherence limited by charge noise and fidelity higher than 99.9%. Nature nanotechnology. 2018;13(2):102–106.
- [30] Noiri A, Takeda K, Nakajima T, Kobayashi T, Sammak A, Scappucci G, et al. Fast universal quantum gate above the fault-tolerance threshold in silicon. Nature. 2022;601(7893):338–342.
- [31] Langrock V, Krzywda JA, Focke N, Seidler I, Schreiber LR, Cywiński L. Blueprint of a Scalable Spin Qubit Shuttle Device for Coherent Mid-Range Qubit Transfer in Disordered Si/SiGe/SiO<sub>2</sub>. PRX Quantum. 2023 Apr;4:020305. https://doi.

- org/10.1103/PRXQuantum.4.020305.
- [32] Cerfontaine P, Botzem T, Ritzmann J, Humpohl SS, Ludwig A, Schuh D, et al. Closed-loop control of a GaAs-based singlet-triplet spin qubit with 99.5% gate fidelity and low leakage. Nature communications. 2020;11(1):4144.
- [33] Hangleiter T, Cerfontaine P, Bluhm H. Filter-function formalism and software package to compute quantum processes of gate sequences for classical non-Markovian noise. Physical Review Research. 2021 Oct;3(4). https://doi.org/10.1103/physrevresearch.3.043047.
- [34] Wardrop MP, Doherty AC. Exchange-based two-qubit gate for singlet-triplet qubits. Phys Rev B. 2014 Jul;90:045418. https://doi.org/10.1103/PhysRevB.90.045418.
- [35] Haarnoja T, Zhou A, Abbeel P, Levine S. Soft actor-critic: Off-policy maximum entropy deep reinforcement learning with a stochastic actor. In: International conference on machine learning. PMLR; 2018. p. 1861–1870.
- [36] Haarnoja T, Zhou A, Hartikainen K, Tucker G, Ha S, Tan J, et al.: Soft Actor-Critic Algorithms and Applications.
- [37] Hiraoka T, Imagawa T, Hashimoto T, Onishi T, Tsuruoka Y.: Dropout Q-Functions for Doubly Efficient Reinforcement Learning. Available from: https://arxiv.org/abs/2110.02034.
- [38] Kuznetsov A, Shvechikov P, Grishin A, Vetrov D. Controlling overestimation bias with truncated mixture of continuous distributional quantile critics. In: International Conference on Machine Learning. PMLR; 2020. p. 5556–5566.
- [39] Pardo F, Tavakoli A, Levdik V, Kormushev P.: Time Limits in Reinforcement Learning. Available from: https://arxiv.org/abs/1712.00378.
- [40] Teske JD, Cerfontaine P, Bluhm H. qopt: An Experiment-Oriented Software Package for Qubit Simulation and Quantum Optimal Control. Physical Review Applied. 2022 Mar;17(3). https://doi.org/10.1103/physrevapplied.17.034036.
- [41] Bezanson J, Edelman A, Karpinski S, Shah VB. Julia: A fresh approach to numerical computing. SIAM Review. 2017;59(1):65–98. https://doi.org/10.1137/141000671.
- [42] Ferrari S, Stengel RF. Smooth function approximation using neural networks. IEEE Transactions on Neural Networks. 2005;16(1):24–38.
- [43] Kingma DP, Ba J. Adam: A method for stochastic optimization. arXiv preprint arXiv:14126980. 2014;.
- [44] Kingma DP, Welling M.: Auto-Encoding Variational Bayes.

- [45] Baldwin CH, Kalev A, Deutsch IH. Quantum process tomography of unitary and near-unitary maps. Physical Review A. 2014;90(1):012110.
- [46] Flammia ST, Silberfarb A, Caves CM. Minimal informationally complete measurements for pure states. Foundations of Physics. 2005;35(12):1985–2006.